Nano ZrO$_2$ particles in nanocrystalline Fe–14Cr–1.5Zr alloy powders

CrossMark

W.Z. Xu, L.L. Li, M. Saber, C.C. Koch, Y.T. Zhu *, R.O. Scattergood

Department of Materials Science and Engineering, North Carolina State University, Raleigh, NC 27695, USA

A R T I C L E   I N F O

A B S T R A C T

Here we report on the formation of nano ZrO$_2$ particles in Fe–14Cr–1.5Zr alloy powders synthesized by mechanical alloying. The nano ZrO$_2$ particles were found uniformly dispersed in the ferritic matrix powders with an average size of about 3.7 nm, which rendered the alloy powders so stable that it retained nanocrystalline structure after annealing at 900 °C for 1 h. The ZrO$_2$ nanoparticles have a tetragonal crystal structure and the following orientation relationship with the matrix: $(002)_{ZrO2}//(002)_{Matrix}$ and $[010]_{ZrO2}//[120]_{Matrix}$. The size and dispersion of the ZrO$_2$ particles are comparable to those of Y–Ti–O enriched oxides reported in irradiation-resistant ODS alloys. This suggests a potential application of the new alloy powders for nuclear energy applications.

© 2014 Elsevier B.V. All rights reserved.

1. Introduction

The resistance of materials to irradiation is one of the key factors that determine the safety, efficiency and service life of the nuclear power plants [1–3]. The next generation nuclear reactors require materials that can not only serve at elevated temperatures but also resist irradiation damage under neutron doses as high as 10–150 displacements per atom (dpa) [4]. Recent findings [5–8] show that it is nano-sized oxides that lead to high creep strength and good irradiation damage tolerance for high temperature operations in ferritic oxide dispersion strengthened (ODS) alloys. Such nano-sized oxides not only act as pinning sites themselves to enhance the creep strength, but also create large amounts of interfacial area, which effectively provides sinks for vacancies, self-interstitials and helium atoms produced by irradiation, thus impeding damage accumulation in the microstructure and improving irradiation resistance [9–11].

Most of nano-sized oxides in current ODS alloys are Y based with Ti added to refine the oxide size at their forming temperature of 1000–1150 °C [5–8,12–15]. These Y–Ti–O enriched oxides are generally divided into two categories based on their size and crystal structure [16]: (i) non-stoichiometric Y–Ti–O enriched oxides (Y/Ti < 1) with sizes in the range of 1–15 nm, and (ii) stoichiometric Y$_2$Ti$_2$O$_7$ with sizes in the range of 15–50 nm. The former is found more effective in enhancing irradiation resistance and creep resistance due to their smaller sizes [17,18]. Similar to Ti, other additions such as Al, Ta or Zr also effectively refine the oxide size

due to the formation of complex oxides with Y [13,19,20]. Although the Y based oxides have been extensively studied for the last decade, little is known whether there exist other type of oxides that have similar ultrafine sizes (<10 nm) and dispersions in the matrix. Such oxide particles may also have the potential to form new ODS alloys with high irradiation resistance.

Nanocrystalline materials, containing large amounts of the interfacial boundaries, also exhibit better irradiation resistance as compared to their coarse-grained counterparts [21–23]. For instance, nanocrystalline Fe film has been found to significantly lower the density of He bubbles under helium irradiation as compared to coarse-grained Fe [24]. Nanocrystalline Pd and ZrO$_2$ have been reported to reduce the defect density by a factor of 3–4 under 4 MeV Kr ion irradiation when their average grain sizes are reduced from 100 nm to 40 nm [25]. However, due to their instability at elevated temperatures, nanocrystalline materials usually undergo grain growth [26,27], which limits their high temperature applications.

In searching for thermally stable nanocrystalline alloys for high temperature applications, our group have synthesized Fe–Cr–Zr [28] and Fe–Zr [29,30] alloys via mechanical alloying. It is found that the Zr addition can help enhance their thermal stability to maintain nanocrystalline structure at 900 °C. This was believed to be caused by the kinetic pinning via the intermetallic compounds and the thermodynamic effects of Zr segregation to the grain boundaries [28–32]. This hypothesis has yet to be verified due to the lack of the detailed microstructure characterization at the atomic resolution.

Here, we report the observation of a high density of nano ZrO$_2$ particles in a nanocrystalline Fe–14Cr–1.5Zr alloy powders, with

* Corresponding author. Tel.: +1 9195130559; fax: +1 9195153419.
E-mail address: ytzhu@ncsu.edu (Y.T. Zhu).

size and dispersion comparable to those oxides in the ODS alloys. They are primarily responsible for the observed high thermal stability of the Fe–14Cr–1.5Zr alloy powders.

2. Experimental procedure

The Fe–14Cr–1.5Zr (at.%) alloy was synthesized by mechanical alloying in a SPEX 8000 M Mixer/Mill. Fe, Cr, and Zr powders with 99.9%, 99.2% and 99.5% purity (from Alpha Aesar), respectively, were used as the starting materials for milling. They were mixed under argon atmosphere and then milled with stainless steel balls for 20 h at room temperature. The ball to powder mass ratio was 10:1. The as-milled powders became a non-equilibrium solid solution, which was further annealed at 900 °C for 1 h under the Ar–2%H$_2$ atmosphere. Note that the composition of the base alloy in the present study (Fe–14Cr) is very similar to a typical ODS alloy (12–20% Cr). Our samples were processed by annealing ball-milled powders, in contrast to conventional ODS alloys, which are typically consolidated by hot isostatic pressing (HIPing) or hot extrusion [5,33,34].

Samples for transmission electron microscopy (TEM) were directly cut from the annealed powder particles using the focused ion beam (FIB) 'lift-out' technique in a FEI Quanta 3D FEG dual-beam instrument. The FIB cut specimen was first thinned by Ga$^+$ ions at 30 keV, followed by 5 keV and 2 keV for the final thinning. TEM images were acquired in a JEM-2010F microscope operated at 200 keV. Energy-dispersive X-ray spectroscopy (EDS) analysis was performed in a aberration-corrected FEI Titan G2 microscope with X-FEG source and ChemiSTEM technology, operated in the scanning transmission electron microscopy (STEM) mode at 200 keV. The probe size of the electron beam is about 0.1 nm in a convergent angle of 21 mrad. The EDS maps of 248 × 208 pixels over an area of 32 × 27 nm were acquired for 1080 s in this study. An annular dark-field detector with an inner angle of 77 mrad was used to obtain the STEM high-angle annular dark-field (HAADF) images. The image contrast in HAADF is proportional to the atomic number (Z), the material density or the sample thickness [35], enabling us to the detect different phases in the microstructure. The electron diffraction patterns of a given crystal structure were simulated using the JEMS software [36].

3. Results

Fig. 1a and b shows typical TEM bright-field and dark-field images of the Fe–14Cr–1.5Zr alloy powders after 1 h annealing at 900 °C. This alloy remains nanocrystalline with an average grain size of about 44 nm (see Fig. 1c) from the measurements of 240 grains. Here, the annealing temperature of 900 °C is about 0.65 T$_m$ of the Fe–14Cr base alloy. Usually, at such a high homologous temperature, nanocrystalline materials are unstable and would undergo rapid grain growth [26]. However, the nanocrystalline structure was retained in this alloy powders, indicating its good thermal stability at elevated temperatures.

Fig. 2a shows a high density of small dot-like dispersoids with dark contrast throughout the grains. These particles are near-equiaxed in shape and are uniformly distributed in the microstructure. The particle size is typically in the range of 1.0–7.5 nm in diameter as shown in the histogram in Fig. 2b. The average size is estimated to be 3.7 nm. More importantly, many of the particles are located near grain boundaries with small inter-particle spacing, which could effectively pin the grain growth, as marked by the arrows in the high resolution TEM image in Fig. 2c.

A compositional analysis of these particles was performed by the energy dispersive X-ray spectroscopy (EDS) elemental mapping. The EDS mapped a region (Fig. 3a) close to the central area of Fig. 2a for major elements such as Fe, Cr, Zr and O, as shown in Fig. 3b–e. It can be seen from the map that these particles are enriched with Zr and O but depleted with Fe. Cr appears distributed around the particle, forming a shell structure. In addition, Cr is also found segregated near some grain boundaries, as indicated by the arrow in Fig. 3c. Quantitative compositional analysis of the dot-like particle is not obtained since the particle is embedded in the matrix and the EDS signals from the particle and the matrix overlapped with each other.

As shown in Fig. 3, nanoparticles are enriched with Zr and O, and are most likely to be zirconium oxides. This is confirmed with the electron diffraction analysis. Fig. 4a shows the selected-area electron diffraction (SAED) pattern of a region that includes both nano-particles and the ferritic matrix. The SAED pattern contains diffraction rings both from nano-particles (marked as red rings) and from the bcc matrix (marked as blue rings). In order to quantitatively show the positions of the diffraction rings, the electron diffraction intensity is further integrated as a function of the ring diameter, and illustrated as peaks covered by the light blue area. It represents the positions of the rings in terms of interplane-spacing in the reciprocal space (nm^{-1}), which could be compared with the simulated electron diffraction results for further phase identification. As seen in Fig. 4b, the positions of peaks from nanoparticles matched the simulated electron diffraction peaks for ZrO$_2$ crystal with a tetragonal structure (space group: P 4$_2$/nmc [37]) as marked by the red line peaks. The electron diffraction from
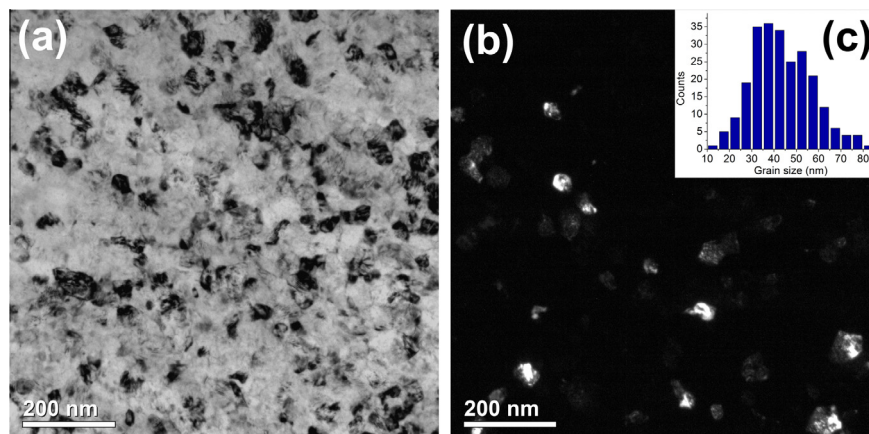

Fig. 1. Microstructure of the Fe–14Cr–1.5Zr alloy after annealing for 1 h at 900 °C. (a) Bright-field and (b) dark-field image in TEM and (c) grain size histogram shows an average grain size of about 44 nm.
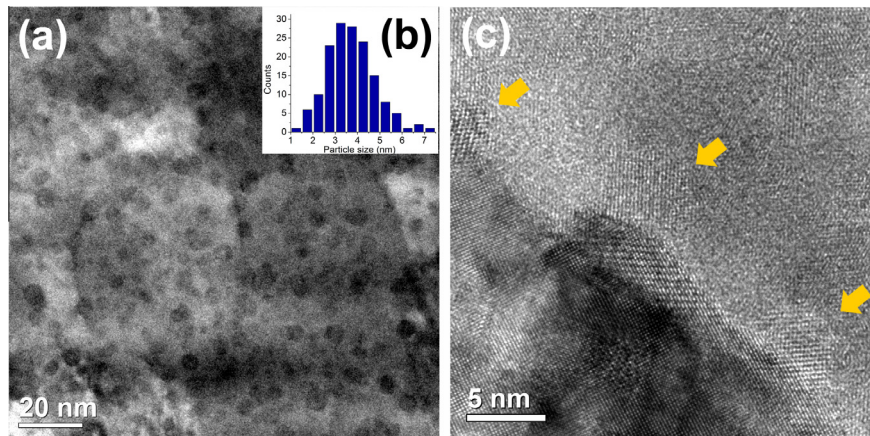
Fig. 2. Formation of nanoparticles in the microstructure. (a) STEM high-angle annular dark-field (HAADF) image. Nanoparticles in dark contrast are uniformly distributed in the matrix. (b) Particle size histogram shows an average size of about 3.7 nm. (c) High-resolution TEM image of a grain boundary region. Some of these particles are located at a grain boundary, as indicated by the yellow arrows. (For interpretation of the references to color in this figure legend, the reader is referred to the web version of this article.)
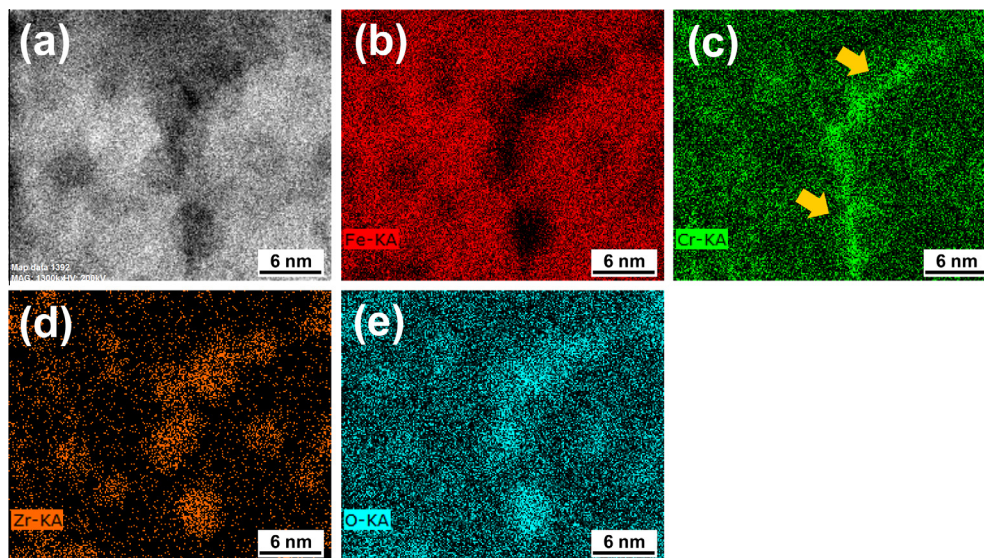

Fig. 3. Energy dispersive X-ray spectroscopy (EDS) elemental mapping of an area near the grain boundary. (a) STEM high-angle annular dark-field (HAADF) image. Elemental mapping of (b) Fe-Kα, (c) Cr-Kα, (d) Zr-Kα and (e) O-Kα. Cr segregation is also found at some of the grain boundaries, as marked by the yellow arrows. (For interpretation of the references to color in this figure legend, the reader is referred to the web version of this article.)

the ferritic matrix in body-centered cubic (bcc) structure is simulated as blue line peaks for comparison.

The tetragonal ZrO_2 phase observed here is known as a high temperature and high pressure phase of ZrO_2 rather than the monoclinic phase (space group: P 2_1/c [38]) of ZrO_2 formed at ambient condition [39]. The electron diffraction of monoclinic ZrO_2 phase was also simulated for comparison as shown by the red line peaks in Fig. 4b, but these peaks failed to match our experimental peaks. The formation of tetragonal ZrO_2 instead of a monoclinic phase here should be largely attributed to its nanometer size [40,41]. Suresh et al. [42] predicted the critical cluster size of a stable tetragonal ZrO_2 at ambient condition to be 15 nm, which is consistent with our findings in this paper.

Fig. 5a shows the high resolution TEM image of a ZrO_2 particle, which is taken along the [010] direction. It appears to have the facet shape bounded by several {002} and {011} interfaces. The corresponding orientations are illustrated on the top right corner of the figure. This particle is actually embedded in a ferritic matrix, where the [010] direction of the ZrO_2 particle is parallel to the [120] direction of the matrix. Interestingly, the (002)

interface of the ZrO_2 and the (002) interfaces of the bcc ferritic matrix are also parallel to each other. The above observations suggest a certain orientation relationship between the ZrO_2 and the matrix:

$$[010]_{ZrO_2}//[1\bar{2}0]_{Matrix}$$
$$(002)_{ZrO_2}//(002)_{Matrix}$$

This kind of relationship for the orientations is clearly revealed by the diffractogram of the image processed by fast Fourier transformation (FFT) in Fig. 5b. Similar to the electron diffraction, the plane normal is parallel to the direction from the center of the diffractogram to the corresponding spot. Fig. 5b includes the 'diffraction' patterns from both the ZrO_2 nano-particle and the matrix, which are indexed in yellow and blue color, respectively. This kind of orientation relationship implies certain semi-coherent type interface along the (002) interface between two phases. This also indicates that nanoparticles should be formed during the annealing process, not mechanically mixed into the matrix during mechanical alloying.
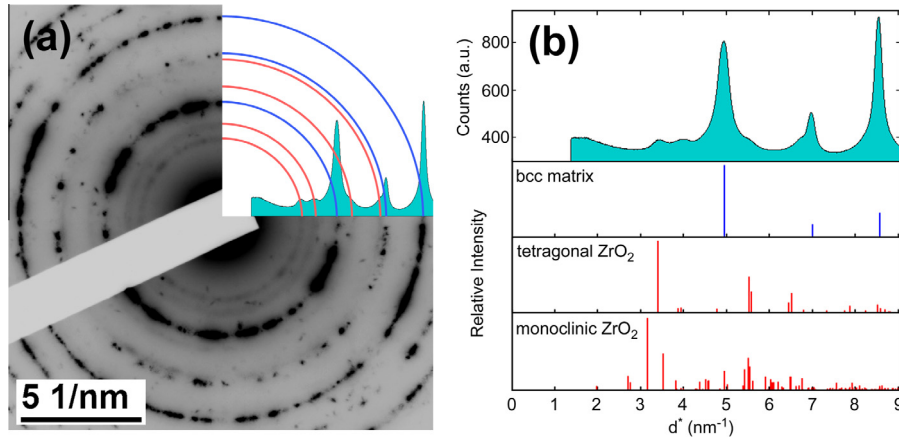
Fig. 4. Electron diffraction analysis of nanoparticles. (a) Selected-area electron diffraction (SAED) pattern containing diffraction rings from both the bcc ferritic matrix (indicated by blue rings) and the nanoparticles (red rings). The electron diffraction intensity was integrated as a function of the ring diameter, as illustrated by peaks covered by the light blue area. (b) Simulated electron diffraction pattern of ZrO_2 in tetragonal and monoclinic crystal structure (red lines) and bcc matrix (blue lines) as a function of the interplane spacing in reciprocal space (nm^{-1}). The simulated pattern of tetragonal ZrO_2 matches well with the experiment data (light blue peaks). (For interpretation of the references to color in this figure legend, the reader is referred to the web version of this article.)
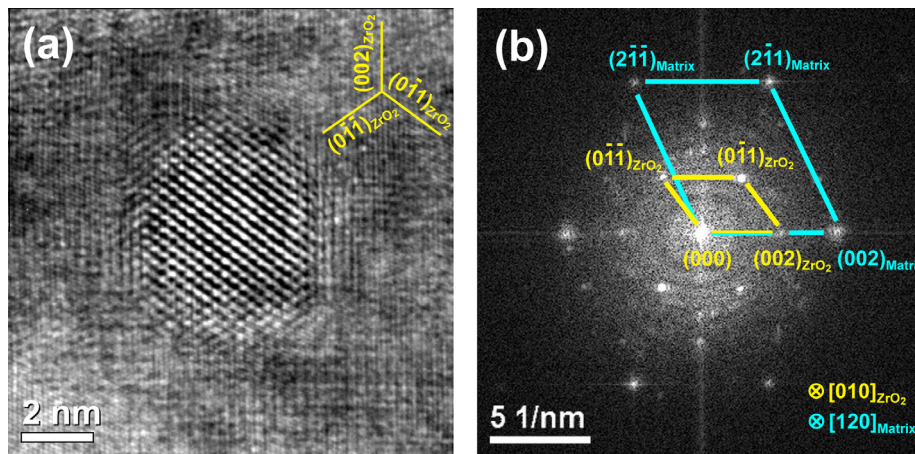

Fig. 5. High-resolution TEM (HRTEM) results of a ZrO_2 particle. (a) HRTEM image of the particle taken along a [010] zone axis. It appears bounded by several {002} and {011} interfaces. The orientation of the interfaces was marked on the top right side. The image also contained the phase contrast from the bcc ferritic matrix along a [120] direction. (b) The fast Fourier transform (FFT) of (a) showing the orientation relationship between the cluster (yellow color) and the matrix (blue color) as $(002)_{ZrO2}//(002)_{Matrix}$ and $[010]_{ZrO2}//[120]_{Matrix}$. (For interpretation of the references to color in this figure legend, the reader is referred to the web version of this article.)

4. Discussion

In this paper, it is found that the formation of the ZrO_2 nanoparticles can help stabilize the nanocrystalline matrix powders during high temperature annealing. This effect can be quantitatively estimated using the Zener equation [43]

$$D = K \frac{d}{f^m} \qquad (1)$$

where D is the estimated grain size due to the pinning effect, d is the size of the pinning particles, f is the volume fraction of particles, K and m are constant. The volume fraction (f) of the ZrO_2 nano-cluster is estimated to be 1.1%, calculated from the STEM results of a region of 36 nm × 36 nm in area and 46 nm in thickness. The STEM image shows a projection image of all nanoparticles along the thickness direction, which enables us to directly calculate the particle volume density. The thickness is measured by electron energy loss spectroscopy (EELS) using the log-ratio method [44]. For $f < 5\%$, $K = 0.17$ and $m = 1$ according to the empirical results obtained using experimental data [43]. Taking the average cluster size $d = 3.7$ nm

in Eq. (1), the estimated grain size (D) is about 57 nm, which is close to our experimental measurements of about 44 nm in Fig. 1c. Here, the smaller grain size of the experimental measurements as compared to the theoretical prediction (in terms of 44 nm vs. 57 nm) might be attributed to the Cr segregation to the grain boundary, which also helps suppress the grain growth [31,45]. This suggests that the high thermal stability of the alloy can be primarily attributed to the grain boundary pinning of nano ZrO_2 particles.

Although oxygen is not purposely added during ball milling, the formation of ZrO_2 particles suggests the existence of oxygen in the powder mixture. Considering the volume fraction (f) of the ZrO_2 to be 1.1%, the weight percent of ZrO_2 could be converted to 0.8%, which corresponds to about 0.2 wt.% of oxygen. The oxygen might partially came from the Zr powder, since Zr has a high affinity for oxygen ($\Delta G_f^\circ = -1037$ kJ/mol [46]) and potentially absorbs oxygen during storage. Moreover, the pre-milled Fe and Cr powders are less than 10 μm in size, which results in large surface areas that also absorb oxygen [47]. The absorbed oxygen is then mechanically alloyed with other elements by ball milling, therefore, allowing the formation of ZrO_2 during the subsequent annealing.

The oxygen content can be controlled by various methods. It can be decreased by either using high purity precursor powders, high purity atmosphere, or performing a degassing process prior to the ball milling [47,48]. On the other hand, the oxygen content might be increased by adding oxygen carriers such as Fe_2O_3 or ZrO_2 [49,50]. At current stage, it is still not clear how the ZrO_2 particle size or density vary with oxygen content, which requires further investigations.

The oxygen concentration in the Fe–14Cr–1.5Zr alloy is higher than the equilibrium oxygen solubility in Fe [51]. It is interesting to mention that a similar scenario is also found in conventional ODS alloys. Both of them are synthesized by the mechanical alloying, and the oxygen content in the latter mostly comes from the Y_2O_3 particles (~0.2–0.3 wt.%) [34], which are mechanically dissolved into the matrix. Studies show that extended solubility of oxygen in ODS alloys is closely related to the high concentration of vacancies, which is introduced by the mechanical alloying process. The strong bonding between the oxygen and vacancies will result in the formation of O-vacancy pairs, thus enabling the existence of excess oxygen in the matrix [52]. The higher oxygen content in Fe–14Cr–1.5Zr alloys is likely caused by this vacancy mechanism considering the same alloy synthesizing process. In addition, the O-vacancy pairs could further attract solutes (such as Ti or Y) with high O affinity and promote the nucleation of O-enriched particles upon heating [52,53]. In fact, the finely dispersed Y–Ti–O enriched oxides are only observed in the ODS alloys [12–15,54] that not only contain a high density of vacancies in microstructure but also have the oxide forming species with high O affinity. Note that Zr and Ti are belongs to the group 4 in the periodic table, and Y is in their neighboring group 3; thus, to some extent, exhibiting quite similar physical or chemical properties. In fact, Zr has high affinity for O, which is similar to Ti and Y. Therefore, the dispersion of nano ZrO_2 particles in the current study is mostly likely attributed to the similar alloying process and the Zr solute addition.

The dispersion of nano ZrO_2 particles observed in the current work is similar to what is observed in ODS alloys. As shown in Fig. 2, the ZrO_2 particles are only about 1.0–7.5 nm in size with an average size of about 3.7 nm. Such small particle sizes are typically categorized into fine oxide range (~1–15 nm) in ODS alloys [12–15]. The smaller particles could produce more effective enhancement for irradiation resistance as well as tensile and creep properties [17,18]. It is also reported that the Y–Ti–O enriched oxides tended to be coherent or semi-coherent with the matrix and had a faceted interface in the smaller particle sizes (<10 nm) [54], which is also consistent with the ZrO_2 particles observed in this study. Here, semi-coherent interface between ZrO_2 and matrix can be seen along the (002) interface, while other interfaces are more likely to be incoherent. In addition, the amount of ZrO_2 (0.8 wt.%) in the matrix is also close to that of Y–Ti–O enriched oxides (0.3–0.7 wt.%). Such a large amount of ZrO_2 therefore effectively stabilizes the nanocrystalline grain at the elevated temperature. With a nanocrystalline matrix and high density of nano ZrO_2 particles, the Fe–14Cr–1.5Zr alloy in the current study is expected to have good irradiation damage resistance.

5. Conclusions

In summary, nano ZrO_2 particles were observed in a Fe–14Cr–1.5Zr (at.%) alloy powders prepared by mechanical alloying and subsequent annealing at 900 °C for 1 h. These particles are uniformly dispersed in the ferritic matrix powders and had an average size of about 3.7 nm. The ZrO_2 particles have a tetragonal crystal structure and a crystallographic orientation relationship with the ferritic matrix as $(002)_{ZrO2}//(002)_{Matrix}$ and $[010]_{ZrO2}//[120]_{Matrix}$.

The thermal stability of the nanocrystalline ferritic matrix alloy powders is largely attributed to the Zener pinning of grain boundaries by the nano-sized, highly dispersed ZrO_2 particles. More importantly, the particle size and dispersion of ZrO_2 particles are comparable to those of Y–Ti–O particles in conventional ODS alloys, suggesting a possible new irradiation resistant material for nuclear energy applications.

References

[1] G.S. Was, J. Nucl. Mater. 367-370 (2007) 11.
[2] R.W. Grimes, R.J.M. Konings, L. Edwards, Nature Mater. 7 (2008) 683.
[3] G. Ackland, Science 327 (2010) 1587.
[4] K.L. Murty, I. Charit, J. Nucl. Mater. 383 (2008) 189.
[5] G.R. Odette, M.J. Alinger, B.D. Wirth, Annu. Rev. Mater. Sci. 38 (2008) 471.
[6] R.L. Klueh, A.T. Nelson, J. Nucl. Mater. 371 (2007) 37.
[7] T. Hayashi, P.M. Sarosi, J.H. Schneibel, M.J. Mills, Acta Mater. 56 (2008) 1407.
[8] S. Ukai, M. Fujiwara, J. Nucl. Mater. 307 (2002) 749.
[9] H. Trinkaus, B.N. Singh, J. Nucl. Mater. 323 (2003) 229.
[10] X.M. Bai, A.F. Voter, R.G. Hoagland, M. Nastasi, B.P. Uberuaga, Science 327 (2010) 1631.
[11] C. Di, J. Wang, T. Chen, L. Shao, Sci. Rep. 3 (2013) 1450.
[12] A. Ramar, N. Baluc, R. Schäublin, J. Nucl. Mater. 386–388 (2009) 515.
[13] L. Hsiung, M. Fluss, S. Tumey, J. Kuntz, B. El-Dasher, M. Wall, B. Choi, A. Kimura, F. Willaime, Y. Serruys, J. Nucl. Mater. 409 (2011) 72.
[14] V. de Castro, T. Leguey, A. Muñoz, M.A. Monge, P. Fernández, A.M. Lancha, R. Pareja, J. Nucl. Mater. 367-370 (2007) 196.
[15] M.K. Miller, K.F. Russell, D.T. Hoelzer, J. Nucl. Mater. 351 (2006) 261.
[16] H. Sakasegawa, L. Chaffron, F. Legendre, L. Boulanger, T. Cozzika, M. Brocq, Y. de Carlan, J. Nucl. Mater. 384 (2009) 115.
[17] D.T. Hoelzer, J. Bentley, M.A. Sokolov, M.K. Miller, G.R. Odette, M.J. Alinger, J. Nucl. Mater. 367-370 (2007) 166.
[18] L.L. Hsiung, M.J. Fluss, S.J. Tumey, B.W. Choi, Y. Serruys, F. Willaime, A. Kimura, Phys. Rev. B 82 (2010) 184103.
[19] X. Mao, T.K. Kim, S.S. Kim, K.H. Oh, J. Jang, J. Nucl. Mater. 428 (2012) 82.
[20] P. Dou, A. Kimura, R. Kasada, T. Okuda, M. Inoue, S. Ukai, S. Ohnuki, T. Fujisawa, F. Abe, J. Nucl. Mater. 444 (2014) 441.
[21] A. Misra, M.J. Demkowicz, X. Zhang, R.G. Hoagland, JOM 59 (2007) 62.
[22] E.G. Fu, J. Carter, G. Swadener, A. Misra, L. Shao, H. Wang, X. Zhang, J. Nucl. Mater. 385 (2009) 629.
[23] I.J. Beyerlein, A. Caro, M.J. Demkowicz, N.A. Mara, A. Misra, B.P. Uberuaga, Mater. Today 16 (2013) 443.
[24] K.Y. Yu, Y. Liu, C. Sun, H. Wang, L. Shao, E.G. Fu, X. Zhang, J. Nucl. Mater. 425 (2012) 140.
[25] M. Rose, A.G. Balogh, H. Hahn, Nucl. Instrum. Meth. B 127–128 (1997) 119.
[26] T.R. Malow, C.C. Koch, Acta Mater. 45 (1997) 2177.
[27] V.Y. Gertsman, R. Birringer, Scripta Metall. Mater. 30 (1994) 577.
[28] M. Saber, H. Kotan, C.C. Koch, R.O. Scattergood, Mater. Sci. Eng. A 556 (2012) 664.
[29] K.A. Darling, B.K. VanLeeuwen, C.C. Koch, R.O. Scattergood, Mater. Sci. Eng. A 527 (2010) 3572.
[30] K.A. Darling, R.N. Chan, P.Z. Wong, J.E. Semones, R.O. Scattergood, C.C. Koch, Scripta Mater. 59 (2008) 530.
[31] M. Saber, H. Kotan, C.C. Koch, R.O. Scattergood, J. Appl. Phys. 113 (2013) 063515.
[32] M. Saber, H. Kotan, C.C. Koch, R.O. Scattergood, J. Appl. Phys. 114 (2013) 103510.
[33] P. Olier, J. Malaplate, M.H. Mathon, D. Nunes, D. Hamon, L. Toualbi, Y. de Carlan, L. Chaffron, J. Nucl. Mater. 428 (2012) 40.
[34] M.J. Alinger, G.R. Odette, D.T. Hoelzer, Acta Mater. 57 (2009) 392.
[35] D.E. Jesson, S.J. Pennycook, Proc. R. Soc. Lond. A 449 (1995) 273.
[36] P.A. Stadelmann, JEMS–EMS java version 2010.
[37] S. Kikkawa, A. Kijima, K. Hirota, O. Yamamoto, J. Am. Ceram. Soc. 85 (2002) 721.
[38] F.J. Torres, J.M. Amigó, J. Alarcón, J. Solid State Chem. 173 (2003) 40.
[39] O. Ohtaka, T. Yamanaka, S. Kume, E. Ito, A. Navrotsky, J. Am. Ceram. Soc. 74 (1991) 505.
[40] G. Skandan, C.M. Foster, H. Frase, M.N. Ali, J.C. Parker, H. Hahn, Nanostruct. Mater. 1 (1992) 313.
[41] H. Zhang, J.F. Banfield, J. Mater. Chem. 8 (1998) 2073.
[42] A. Suresh, M.J. Mayo, W.D. Porter, C.J. Rawn, J. Am. Ceram. Soc. 86 (2003) 360.
[43] P.A. Manohar, M. Ferry, T. Chandra, ISIJ Int. 38 (1998) 913.
[44] T. Malis, S.C. Cheng, R.F. Egerton, J. Electron Microsc. Tech. 8 (1988) 193.

[45] T. Chookajorn, H.A. Murdoch, C.A. Schuh, Science 337 (2012) 951.
[46] D.R. Lide, CRC Handbook of Chemistry and Physics, Internet Version ed., CRC Press, Boca Raton, Florida, 2005.
[47] Z. Oksiuta, N. Baluc, Nucl. Fusion 49 (2009) 055003.
[48] S. Ohtsuka, S. Ukai, M. Fujiwara, T. Kaito, T. Narita, J. Phys. Chem. Solids 66 (2005) 571.
[49] Y. Wen, Y. Liu, F. Liu, T. Fujita, D. Liu, M. Chen, B. Huang, J. Nucl. Mater. 405 (2010) 199.
[50] M. Brocq, B. Radiguet, J.M. Le Breton, F. Cuvilly, P. Pareige, F. Legendre, Acta Mater. 58 (2010) 1806.
[51] J.H. Swisher, E.T. Turkdogan, Trans. Metall. Soc. AIME 239 (1967) 426.
[52] C.L. Fu, M. Krčmar, G.S. Painter, X.-Q. Chen, Phys. Rev. Lett. 99 (2007) 225502.
[53] X.L. Wang, C.T. Liu, U. Keiderling, A.D. Stoica, L. Yang, M.K. Miller, C.L. Fu, D. Ma, K. An, J. Alloys Compd. 529 (2012) 96.
[54] A. Hirata, T. Fujita, Y.R. Wen, J.H. Schneibel, C.T. Liu, M.W. Chen, Nat. Mater. 10 (2011) 922.